

# Far-Infrared Transition and Diffraction Radiation Part II: The THz Beamline at the VUV-FEL Linac

Sara Casalbuoni<sup>1\*</sup>, Bernhard Schmidt<sup>1</sup>, Peter Schmüser<sup>1,2</sup>, Bernd Steffen<sup>1,2</sup>

1 Deutsches Elektronen-Synchrotron DESY

2 Institut für Experimentalphysik, Universität Hamburg

\* Present address: Institut für Synchrotronstrahlung, Forschungszentrum Karlsruhe

## 1 Introduction

The Vacuum Ultraviolet Free-Electron Laser (VUV-FEL) at DESY has recently been upgraded to a maximum electron energy of 700 MeV, allowing to cover the wavelength range from 13 to 100 nm. The FEL is based on the principle of Self Stimulated Spontaneous Emission (SASE) which opens the way to powerful FELs in the X ray regime. Electron bunches of extremely high local charge density are needed to achieve laser saturation in the 27 m long undulator magnet. The 1 nC electron bunches are generated in an rf photocathode with an rms length of 5 ps and are rapidly accelerated to relativistic energies to reduce the emittance dilution due to internal space charge forces. At energies of 125 resp. 380 MeV the bunches are longitudinally compressed to a narrow peak with an rms pulse length of  $\sigma_t < 100$  fs which is followed by a longer tail. A schematic view of the VUV-FEL is shown in Fig. 1.

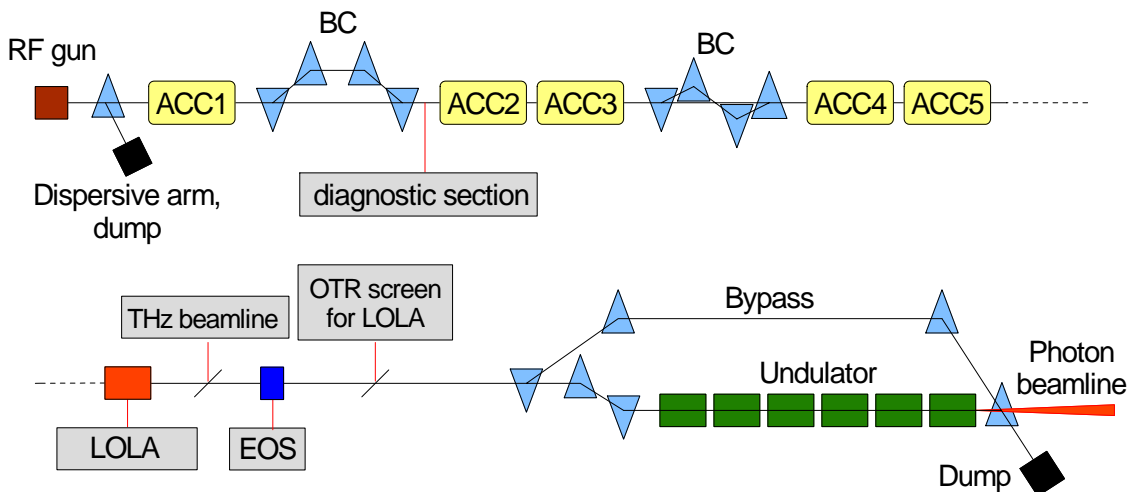


Figure 1: Schematic layout of the VUV-FEL at DESY. The beam is accelerated to a maximum energy of 700 MeV in five acceleration modules ACC1 to ACC5, each containing eight superconducting cavities. The two bunch compression stages are denoted by BC. The special vacuum chamber of the THz beamline containing the screens for transition and diffraction radiation and a diamond exit window is located between the transverse deflecting RF structure LOLA and the electro-optic experiment EOS.

Precise measurements of the temporal profile of the compressed electron bunches are essential for the optimization of the linac and a proper understanding of the bunch compression mechanism including subtle effects such as coherent synchrotron radiation in the magnetic chicanes of the bunch compressor (BC) magnets. Theoretical investigations have shown that this radiation might lead to the evolution of a micro-bunch structure in the BC magnets with a periodicity in the 5 - 10  $\mu\text{m}$  range, see the thesis by F. Stulle [1] and the literature quoted therein. Coherent transition radiation with wavelengths in the infrared and far-infrared regime from about 5  $\mu\text{m}$  to 1000  $\mu\text{m}$  is a suitable tool for a detailed study of the longitudinal charge profile of the electron bunches.

In order to facilitate longitudinal bunch diagnostics with high-resolution interferometric or spectroscopic devices outside the VUV-FEL tunnel we have designed a Tera-Hertz beamline at the 140 m position of the VUV-FEL linac. The vacuum chamber housing the transition and diffraction radiation screens is located between the last acceleration module and the collimator section in front of the undulator. In Part I of this report [2] we have presented a general scheme for computing the generation, diffraction and optical propagation of transition and diffraction radiation. In the present Part II we describe the design, technical layout and optical performance of the THz beamline at the VUV-FEL and show first measurements.

## 2 Basic Design Criteria of the THz Beamline

The purpose of the THz beamline is to transport coherent transition (CTR) or coherent diffraction radiation (CDR) from the linear accelerator over a distance of 18.6 m to an experimental hut. A major constraint is a 9 m long pipe of about 200 mm diameter through which the radiation has to be guided to cross the shielding wall of the accelerator. The design of the THz transfer line has been governed by the following considerations.

- To preserve the temporal structure of the electron bunches a flat frequency response is an important criterion. For this purpose a diamond window is used to couple the radiation from the Ultra High Vacuum (UHV) environment of the linear electron accelerator into the THz transfer line. Diamond is the only material featuring a high transmission without any resonant absorption in the wavelength range from about 6  $\mu\text{m}$  to several mm.
- The transfer line must be evacuated to less than 0.1 mbar to avoid the water vapor absorption lines which would strongly distort the frequency spectrum in a transfer channel filled with air of normal humidity.
- To obtain a high transfer efficiency the optics of the transfer line must be carefully designed and especially optimized for the long wavelength region where diffraction widens up the beam considerably. The focusing of the THz beam should only be done with concave mirrors because lenses made from any material other than diamond would absorb almost all radiation above 4 THz. The restriction to focusing mirrors has a strong implication for the optical layout because it prevents the use of a focusing element in the 9 m long section where the THz beamline crosses the accelerator shielding wall.

## 2.1 Vacuum window at the accelerator

The vacuum window should be made from a material that is transparent to THz radiation over a wide range of frequencies. Conventional window materials for THz applications are low-density polyethylene LDPE and single-crystal quartz. The best choice, however, is chemical vapor deposition (CVD) diamond [3]. In Fig. 2 the transmission coefficients of the three window materials is plotted as a function of wavelength. The intensity transmission coefficient  $T(\lambda)$  has been calculated as a function of wavelength from measured data on the refractive index  $n(\lambda)$  and the extinction coefficient  $\kappa(\lambda)$ , reported for diamond in Ref. [3] and for crystalline quartz and low-density polyethylene in Ref. [4].

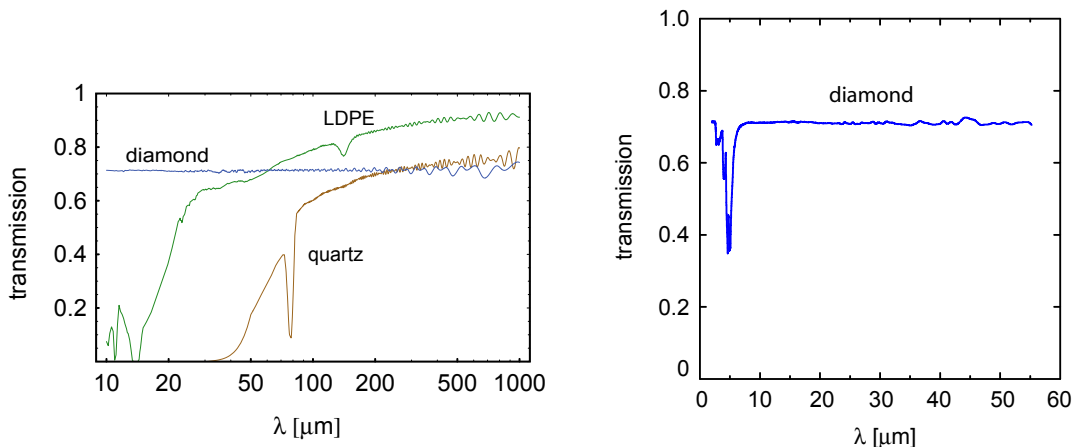


Figure 2: *Left: Intensity transmission coefficient as a function of wavelength for a 0.5 mm thick window made from CVD diamond, low-density polyethylene LDPE or single-crystal quartz. Right: Transmission through a 0.5 mm thick CVD diamond window at small wavelengths. Note that the absorption in diamond is negligible above 7  $\mu\text{m}$ , the observed intensity reduction of  $\approx 29\%$  is caused by reflection losses at the front resp. back surface of the window.*

## 2.2 THz absorption in humid air

Air with normal humidity has a high absorption for THz radiation [5] as can be seen from Fig. 3. To obtain a wavelength-independent transfer efficiency the beamline needs to be evacuated to a pressure of less than 0.1 mbar.

## 2.3 Optical layout of the beamline

The transport of a Gaussian laser beam over a distance  $D$  is conveniently done with two lenses of focal length  $f_1 = f_2 = D/4$ , which are placed at the positions  $z_1 = D/4$  and  $z_2 = 3D/4$ . The transfer matrix of this system is the negative unit matrix, so a beam waist at the laser output is imaged to a waist of the same size at the observation plane  $z = D$ . The boundary conditions at the VUV-FEL require a deviation from this ideal optical setup because it is not possible to install focusing mirrors in the 9 m long section inside the shielding wall. More importantly, in order to cope with the strong widening of

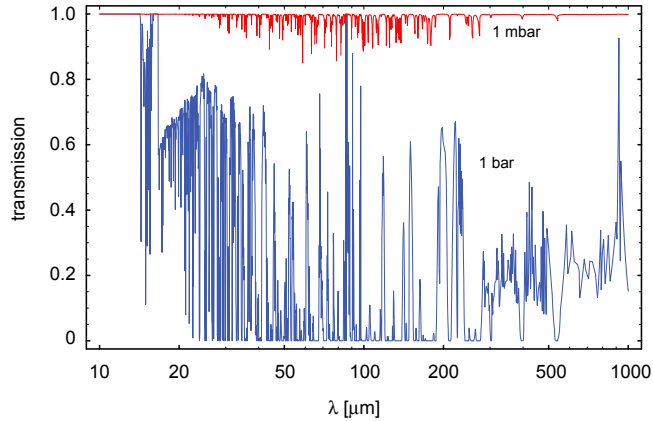


Figure 3: Transmission through 20 m of air with 50% relative humidity as a function of wavelength. The pressure is 1 bar (blue) resp. 1 mbar (red).

the THz beam at long wavelengths, the first focusing element of the transfer line has to be positioned at a much closer distance from the radiation screen than  $z_1 = D/4 = 4.7$  m, because otherwise the limited beam pipe radius of 100 mm would strongly suppress the long wavelength components<sup>1</sup>.

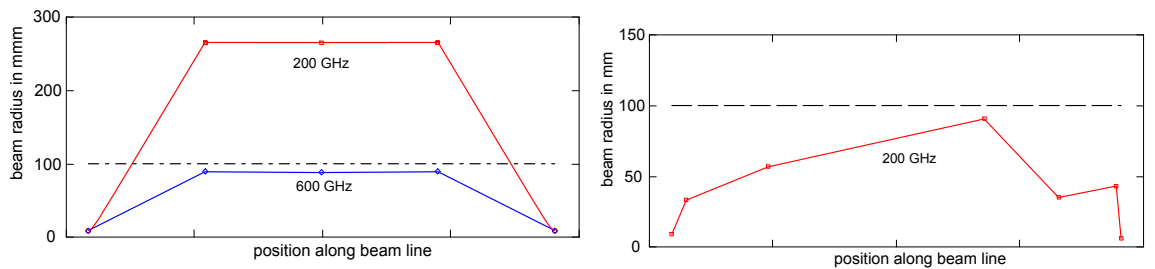


Figure 4: Left graph: Transport of a Gaussian beam with frequency  $f = 200$  GHz (red squares) resp.  $f = 600$  GHz (blue diamonds) through a beamline of length  $D = 18.6$  m. The focusing is provided by two lenses of focal length  $f_1 = f_2 = D/4$ , which are placed at the positions  $z_1 = D/4$  and  $z_2 = 3D/4$ . The initial waist radius is  $w_0 = 9$  mm. The envelope of the beam is sketched. The radius of the beampipe of 100 mm is indicated by the dash-dotted line. Right graph: Transport of a 200 GHz Gaussian beam through a five-lense arrangement according to Fig. 5.

This is demonstrated in Fig. 4, where the envelope of a Gaussian beam is plotted schematically for a frequency  $f = 200$  GHz and an initial beam waist radius  $w_0 = 9$  mm. One can see that the beam radius exceeds the transfer line pipe radius  $r_{pipe} = 100$  mm by more than a factor of two. For this reason more than two focusing elements are needed.

<sup>1</sup>Initially it was planned to use a stainless steel pipe with an inner radius of 100 mm. Later the decision was taken to replace the smooth pipes by bellows of 96 mm inner radius in order to suppress waveguide effects in the THz beamline, see Sect. 4.3.

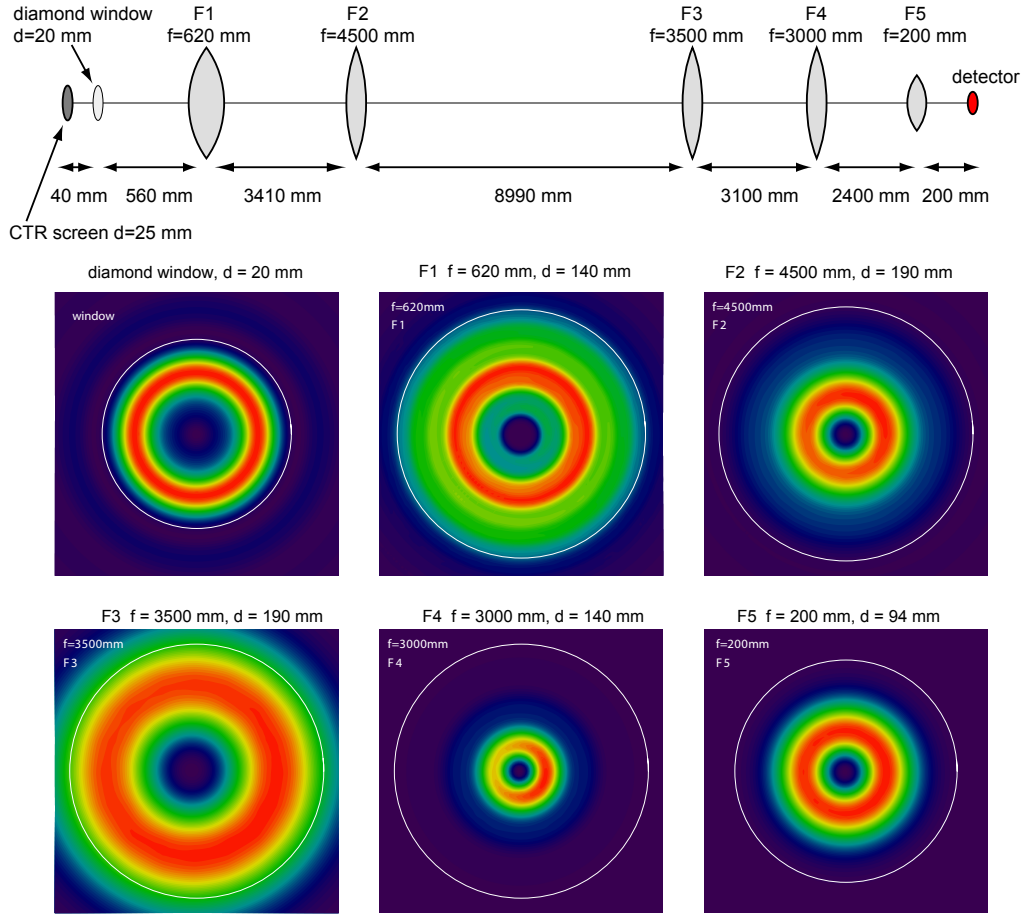


Figure 5: Top row: Schematic optical design of the THz transfer line. The focusing elements  $F1$  to  $F5$  are shown as lenses with their respective positions and focal lengths. Middle and bottom row: The two-dimensional intensity distributions at the diamond window and the five focusing elements  $F1$  to  $F5$ . These are treated as ideal thin lenses, in reality they are toroidal mirrors, see Sect. 4. The circles indicate the free aperture of each element. The diameters  $d$  are listed on top of the pictures. The generation and propagation of transition radiation with a frequency  $f = 200$  GHz (wavelength 1.5 mm) has been modeled using the program *THzTransport* [6]. The Lorentz factor of the electrons is  $\gamma = 1000$ .

From our simulations<sup>2</sup> we find that a beam line with five focusing elements reduces the maximum radius of the Gaussian beam to less than 100 mm.

A schematic view of the beamline optics is shown in Fig. 5, the envelope of a Gaussian beam with  $f = 200$  GHz and  $w_0 = 9$  mm is sketched in Fig. 4. The optical performance for transition radiation at 200 GHz is demonstrated in Fig. 5 for slightly idealized conditions: (1) the  $45^\circ$  inclination angle of the radiation screen with respect to the electron beam is ignored, so effectively we look here at backward transition radiation; (2) the diamond win-

<sup>2</sup>The optimization of the THz beamline optics has been made for transition radiation instead of a Gaussian beam. However, an important design goal was to achieve good transfer efficiency for Gaussian beams, too.

dow at a distance of 40 mm from the CTR screen is simply treated as a circular aperture of 20 mm diameter, the reflection losses at the diamond-vacuum interfaces are neglected; (3) the focusing elements are treated as ideal lenses. With these simplifications, the code *THzTransport* [6] has been used to compute the electromagnetic field pattern and the two-dimensional intensity distributions at the window and the positions of the five focusing elements. The realistic computation of the THz beamline will be presented in Sect. 4. From Fig. 5 it is obvious that the element F3 with a diameter of 190 mm constitutes the tightest aperture limitation at low frequency. A sizable fraction of the 200 GHz beam is not accepted by this aperture. This conclusion will remain valid for the realistic beam line.

In addition to transition radiation we have also studied the beamline properties for a linearly polarized Gaussian beam at  $f = 200$  GHz. As shown in Fig. 6, the Gaussian beam is transported through the beamline with a higher efficiency than the TR beam, which is understandable because this beam has its intensity maximum on the optical axis where the transition radiation intensity vanishes due to destructive interference.

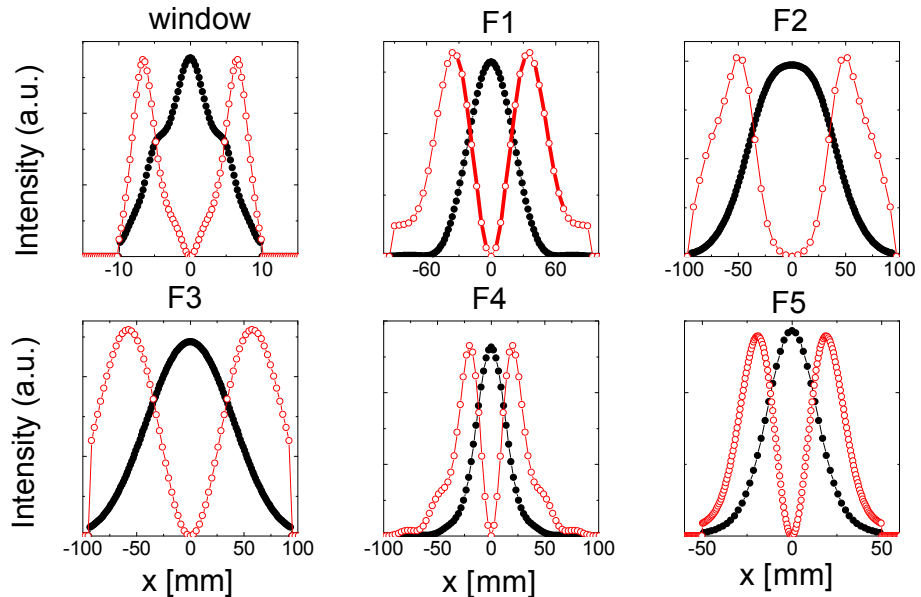


Figure 6: Radiation intensity at the different elements of the THz beamline (diamond window, focusing elements F1 to F5), plotted as a function of the horizontal coordinate  $x$  at the midplane  $y = 0$  of each element. The frequency is 200 GHz. A comparison is made between transition radiation (red) and a Gaussian beam with an initial waist radius  $w_0 = 9$  mm (black).

### 3 Numerical computation of THz wave propagation and diffraction

#### 3.1 Simulation tools

The transport of transition and diffraction radiation in the THz regime has been simulated with two codes:

- ZEMAX, a commercially available program for the design of optical systems [7]
- *THzTransport*, a program written in Mathematica by B. Schmidt [6].

#### 3.2 Kirchhoff regime

For distances  $D$  that are much larger than the dimensions of the image, both programs make use of the so-called physical optics propagation. The geometry is shown in Fig. 7. According to Part I of this report, the horizontal component of the Fourier-transformed

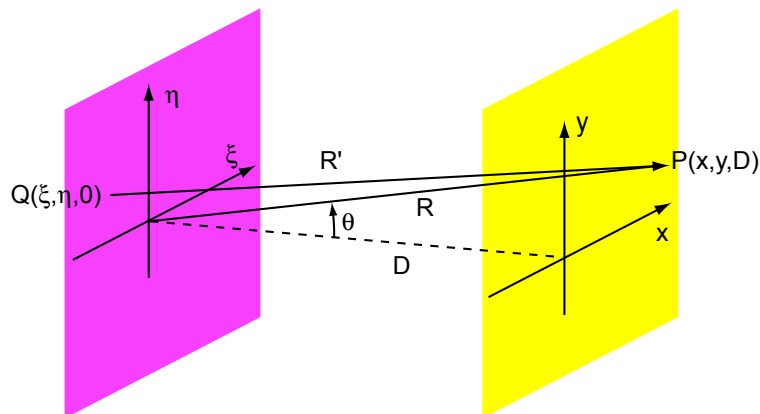


Figure 7: Geometry of source screen and observation screen.

electric field at the point  $P = (x, y, D)$  on the observation screen is given in terms of the horizontal field component on the source screen by the following expression

$$\begin{aligned} \tilde{E}_x(P, \omega) &= -\frac{ik}{2\pi} \frac{\exp(i\omega D/c)}{D} \exp\left(\frac{i\omega(x^2 + y^2)}{2Dc}\right) \\ &\times \int \int \tilde{E}_x(Q, \omega) \exp\left(\frac{i\omega(\xi^2 + \eta^2)}{2Dc}\right) \exp[-i(k_x\xi + k_y\eta)] d\xi d\eta \quad (1) \end{aligned}$$

where  $Q = (\xi, \eta, 0)$  is the general point on the source screen,  $k = 2\pi/\lambda = \omega/c$  the wave number and  $k_x = kx/D$ ,  $k_y = ky/D$ . A corresponding expression holds for the vertical field component. The Fourier integral (1) contains the phase factor  $\exp(ik(\xi^2 + \eta^2)/(2D))$  and can therefore describe both far-field and near-field diffraction (see Part I). A Fast Fourier Transform (FFT) algorithm is used to evaluate the integral.

### 3.3 Angular spectrum propagation

For distances  $D$  which are in the order of the image dimensions the angular spectrum propagation [8, 9, 10] leads to more realistic results than the physical optics propagation. The complex electric field distribution on the source screen is expanded into a sum of plane waves, which are individually propagated to the observation screen and then re-summed. A plane wave can be written as

$$\exp(i(k_x x + k_y y + k_z z))$$

where the  $k_i$  are the components of the wave vector  $\mathbf{k}$  and  $k = |\mathbf{k}| = 2\pi/\lambda = \omega/c$  is the wave number. In the paraxial approximation the angles with respect to the main direction of propagation, taken as the  $z$  direction, are small. Then  $|k_x|, |k_y| \ll k$  and

$$k_z = \sqrt{k^2 - k_x^2 - k_y^2} \approx k - \frac{k_x^2 + k_y^2}{2k}$$

For each frequency component, the horizontal (vertical) electric field on the source screen is subjected to a two-dimensional transverse Fourier transformation. The Fourier components  $F_{x,y}(\omega, k_x, k_y, z)$  depend on the frequency  $\omega = 2\pi f$ , the transverse Fourier-space coordinates  $k_x, k_y$ , and on the longitudinal spatial coordinate  $z$ . At the position  $z = 0$  of the source screen they are given by

$$F_x(\omega, k_x, k_y, 0) = \frac{1}{2\pi} \underbrace{\int \int}_{\text{source screen}} \tilde{E}_x(\xi, \eta, \omega) \exp(-i(k_x \xi + k_y \eta)) d\xi d\eta \quad (2)$$

$$F_y(\omega, k_x, k_y, 0) = \frac{1}{2\pi} \underbrace{\int \int}_{\text{source screen}} \tilde{E}_y(\xi, \eta, \omega) \exp(-i(k_x \xi + k_y \eta)) d\xi d\eta \quad (3)$$

The Fourier components are now propagated as plane waves to the observation screen at  $z = D$ :

$$\begin{aligned} F_x(\omega, k_x, k_y, D) &= \exp(ik_z D) F_x(\omega, k_x, k_y, 0) \\ &= \exp\left(\frac{i\omega D}{c}\right) \exp\left(-\frac{i(k_x^2 + k_y^2)Dc}{2\omega}\right) F_x(\omega, k_x, k_y, 0) \end{aligned} \quad (4)$$

and similarly for  $F_y(\omega, k_x, k_y, 0)$ . The electric field at the observation point  $P = (x, y, D)$  is then computed by an inverse Fourier transformation

$$\tilde{E}_x(\omega, x, y) = \frac{1}{2\pi} \int \int F_x(\omega, k_x, k_y, D) \exp(i(k_x x + k_y y)) dk_x dk_y \quad (5)$$

$$\tilde{E}_y(\omega, x, y) = \frac{1}{2\pi} \int \int F_y(\omega, k_x, k_y, D) \exp(i(k_x x + k_y y)) dk_x dk_y \quad (6)$$

It has been verified that for medium distances both methods (physical optics propagation and angular spectrum propagation) lead to identical results<sup>3</sup>.

<sup>3</sup>Mathematically, both methods are equivalent but in numerical computations the accuracy is better if one uses the first method for large distances and the second one for small distances.

## 4 Technical layout and optical properties of the THz beamline

The main components of the THz beamline are: a special UHV chamber in the linac containing the transition and diffraction radiation screens, a diamond exit window, an evacuated transfer channel equipped with five focusing mirrors F1 to F5 and four plane mirrors P1 to P4. The arrangement of the mirrors is shown in Fig. 8. The final component is a large vacuum vessel for carrying out interferometric, spectroscopic or electro-optic experiments utilizing the full THz spectrum. Alternatively, the radiation can be coupled out of the transfer line vacuum pipe through a single-crystal quartz window for experiments in air, however at the price of a strong suppression of the frequencies above 4 THz, due to the absorption in quartz. The beam line was installed in August 2005 and is presently being used for bunch diagnostics with THz spectroscopy.

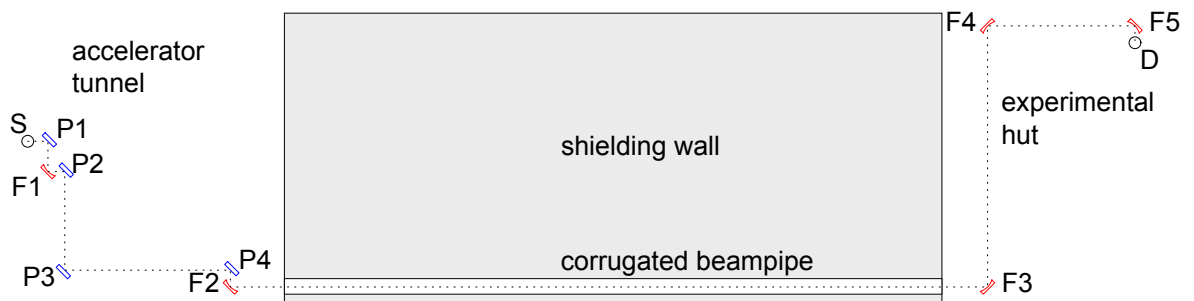


Figure 8: *Layout of the THz beamline with transition radiation screen  $S$ , five focusing mirrors  $F1$  to  $F5$ , four plane mirrors  $P1$  to  $P4$ , and detector  $D$ . The sketch is somewhat simplified. In reality, the optical path between the mirrors  $F1$  and  $P2$  and between  $F4$  and  $F5$  is perpendicular to the plane of the drawing. Thereby the polarization of the radiation is rotated by  $90^\circ$ .*

### 4.1 Diamond window

Since the price of CVD diamond windows increases very rapidly with size it was decided to use a small window with a radius  $r_{win} = 10$  mm and place it at the closest possible distance to the CTR screen. The minimum distance which appeared feasible was  $D_w = 40$  mm. A photo of the diamond window is shown in Fig. 9.

#### 4.1.1 Multiple reflections in the window - parallel faces

The refractive index of CVD diamond is  $n_0 = 2.38$  for wavelengths above  $10 \mu\text{m}$  [3]. We first look at a diamond slab of thickness  $d_0$  with plane parallel faces. At the entrance resp. exit surface of the diamond slab, part of the incident THz wave is transmitted, the other part is reflected. The amplitude transmission coefficients  $T_1$  at the interface from vacuum to diamond and  $T_2$  at the interface from diamond to vacuum are

$$T_1 = \frac{2}{n_0 + 1}, \quad T_2 = \frac{2n_0}{n_0 + 1}$$



Figure 9: View through the diamond window onto the transition radiation screen. The red spot is light from an alignment laser. The window was fabricated by Diamond Materials GmbH, Freiburg.

The amplitude reflection coefficient for the transition from diamond to vacuum is

$$R = \frac{n_0 - 1}{n_0 + 1}$$

Call  $E_0$  the electric field of the THz wave just before entering the diamond slab. The transmitted field just behind the front surface is then

$$E_1 = T_1 E_0$$

Propagation through the slab of thickness  $d_0$  and refractive index  $n_0$  introduces the phase factor  $\exp(in_0 k d_0)$  where  $k = 2\pi/\lambda = \omega/c$  is the wave number in vacuum and  $n_0 k$  the wave number in diamond. Neglecting multiple reflections (first-order calculation), the field leaving the slab is

$$E_2^{(1)} = T_2 E_1 \exp(in_0 k d_0) = \frac{4n_0}{(n_0 + 1)^2} \exp(in_0 k d_0) E_0$$

Note that the absorption in diamond is negligible. Now we take internal reflections into account. The second-order contribution is

$$E_2^{(2)} = T_1 E_0 \exp(in_0 k d_0) R \exp(in_0 k d_0) R \exp(in_0 k d_0) T_2 = q \cdot E_2^{(1)}$$

where the complex coefficient

$$q = \left( \frac{n_0 - 1}{n_0 + 1} \right)^2 \exp(i2 n_0 k d_0)$$

accounts for the reflections at the back and front surface and for the propagation through twice the thickness of the diamond slab. Summation over all orders yields for the field behind the diamond slab

$$E_2 = E_2^{(1)}(1 + q + q^2 + q^3 \dots) = \frac{E_2^{(1)}}{1 - q} = \frac{4n_0 \exp(in_0 k d_0)}{(n_0 + 1)^2 - (n_0 - 1)^2 \exp(i2 n_0 k d_0)} \cdot E_0$$

The transmitted THz energy, normalized to the incident energy, is

$$\begin{aligned} \frac{U_{trans}}{U_0} &= \left| \frac{E_2}{E_0} \right|^2 = \frac{16n_0^2}{|(n_0 + 1)^2 - (n_0 - 1)^2 \exp(i2 n_0 k d_0)|^2} \\ &= \frac{8n_0^2}{n_0^4 + 6n_0^2 + 1 - (n_0^2 - 1)^2 \cos(2n_0 k d_0)} \end{aligned} \quad (7)$$

This energy transmission ratio is plotted in Fig. 10 as a function of frequency. One

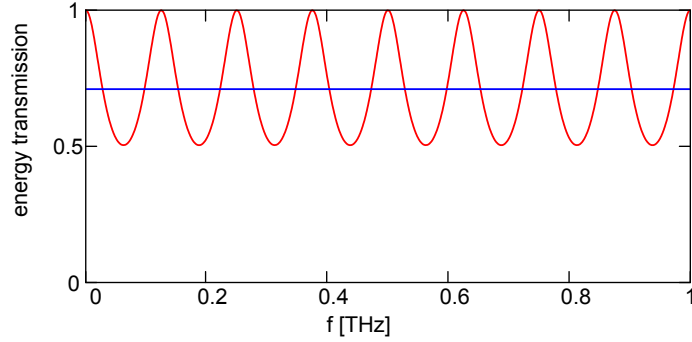


Figure 10: *Ratio of transmitted to incident energy as a function of frequency for a plane-parallel CVD diamond window with a thickness of 0.5 mm. The average energy transmission ratio is 0.71 (blue line).*

observes strong oscillations between 50% and 100%. The average energy transmission ratio is 71%.

#### 4.1.2 Multiple reflections in the window - wedge-shaped window

The undesirable oscillations in the transmitted THz energy can be suppressed by using a window of variable thickness. It is technically feasible to grind a CVD diamond window with a wedge angle  $\alpha_{wedge} = 1^\circ$ . Assuming that the incident THz beam covers the 20 mm diameter of the window with nearly uniform intensity we obtain the energy transmission ratio plotted in Fig. 11. Except for frequencies below 200 GHz the transmission is almost frequency-independent and has the value of 71% quoted above. The window used in the THz beamline has been produced with this wedge angle of  $1^\circ$ .

Another effect of the wedge is the deflection of the beam. The window acts as a prism which deflects the direct ray by an angle

$$\varphi_{dir} = (n_0 - 1)\alpha_{wedge} = 14.7 \text{ mrad}$$

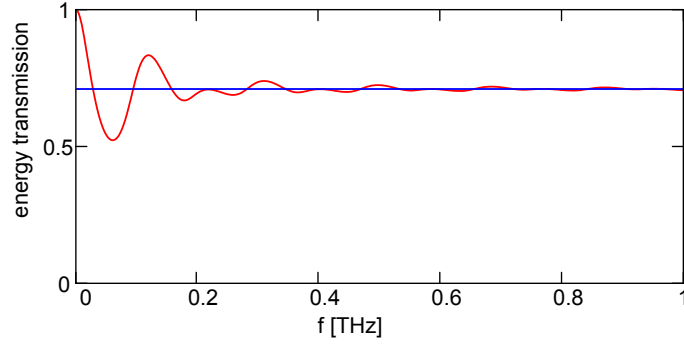


Figure 11: Ratio of transmitted to incident THz energy as a function of frequency for a CVD diamond window with a wedge angle  $\alpha_{wedge} = 1^\circ$ . The mean thickness is 0.5 mm.

The double-reflected ray is deflected by

$$\varphi_{double} = (3n_0 - 1)\alpha_{wedge} = 65 \text{ mrad}$$

Hence the beams are spatially separated at the first focusing mirror F1 of the beamline which is positioned at a distance of 600 mm. The distribution of the directly transmitted intensity on mirror F1 is shown in Fig. 12 for transition radiation with a frequency of 1 THz. Also shown are the intensity distributions for multiple reflections inside the diamond window. The radius of mirror F1 is 70 mm, so we infer from Fig. 12 that a

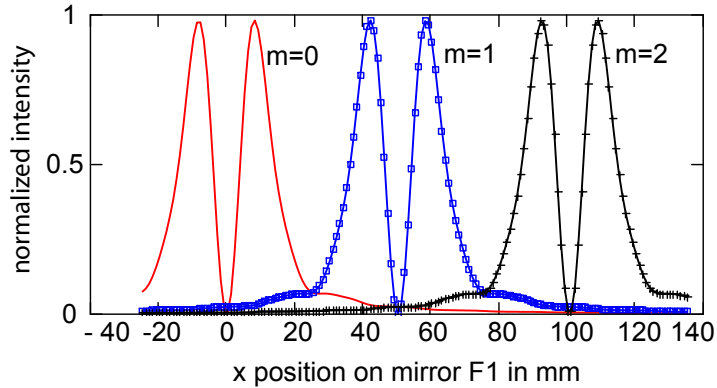


Figure 12: Intensity of transition radiation at  $f = 1 \text{ THz}$  as a function of the horizontal coordinate  $x$  on mirror F1. Red curves: direct transmission of the wedge-shaped diamond window ( $m = 0$ ), blue squares: double reflection in the window ( $m = 1$ ), black crosses: 4 reflections in the window ( $m = 2$ ). All distribution are normalized to a maximum of 1. In reality the double reflection is suppressed by a factor of  $|q|^2 = 0.17$  and the fourfold reflection by factor of  $|q|^4 = 0.03$ .

large fraction of the double-reflected intensity will be accepted by the mirror. Generally, a beam with  $2m$  internal reflections will be deflected by the angle

$$\varphi_{2m} = [(2m + 1)n_0 - 1]\alpha_{wedge}$$

which already for  $m = 2$  exceeds the acceptance angle of mirror F1. However, the terms with  $m > 1$  contribute very little to the transmitted intensity. Hence the oscillatory pattern in the transmitted intensity is predominantly caused by the interference between the two terms  $m = 0$  and  $m = 1$ . The main effect in smearing out this interference is due to the variable thickness and not due to the spatial separation.

## 4.2 Screens for the generation of coherent THz radiation

### 4.2.1 Size of the CTR screen

The dimension of the CTR screen is constrained by the small aperture of the diamond window. The window has a radius  $r_w = 10$  mm and is placed at the closest possible distance of 40 mm from the electron beam. For  $\gamma = 1000$  and a frequency of 200 GHz we have calculated the transition radiation intensity at the window for a circular CTR screen with a radius  $a$  between 5 and 20 mm. For simplicity the calculations have been done for backward transition radiation. The results are presented in Fig. 13. There is perfect agreement between the codes ZEMAX and *THzTransport*. Based on these calculations we

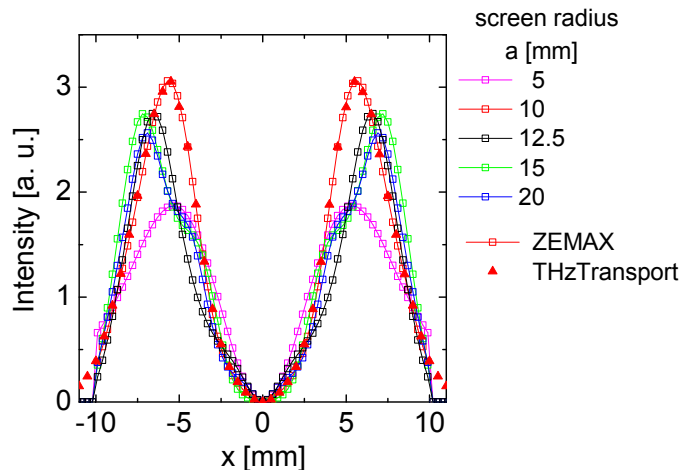


Figure 13: *Horizontal intensity distribution of transition radiation on the diamond window. The CTR screen radius  $a$  is varied between 5 and 20 mm.*

come to the conclusion that the best choice is a screen radius  $a$  between 10 and 12.5 mm. In reality the screen has an inclination angle of  $45^\circ$  with respect to the electron beam direction, so it should have an elliptical shape with a short half axis of 12.5 mm and a long half axis of 17 mm to appear as a circle to the incident beam.

### 4.2.2 Technical layout of the transition and diffraction radiation screens

Four different screens are installed to produce coherent radiation for beam diagnostics:

- (1) a full screen for coherent transition radiation (CTR)
- (2) a coherent diffraction radiation (CDR) screen with a central 4 mm hole to permit beam diagnostics with a long train of electron bunches during FEL operation

- (3) a slit-type diffraction radiator with 4 mm slit width
- (4) an off-axis screen, positioned outside the electron beam, which serves as a transition radiator by steering selected electron bunches onto this screen using a kicker magnet

For technical reasons these screens have been fabricated with a rectangular shape instead of the ideal elliptical shape discussed above. The screens are made from 380  $\mu\text{m}$  thick polished silicon wafers and covered with a 150 nm thick aluminum layer. The CTR screen has a size of  $36 \times 25 \text{ mm}^2$  such that it appears to the incident electron beam as a square of 25 mm side length instead of the ideal circle of 25 mm diameter.

The CTR screen 1 intercepts the electron beam and allows to observe THz radiation from 0.2 to 50 THz but also optical transition radiation for alignment or timing purposes. This screen cannot be used during FEL operation because it would spoil the electron beam emittance. In contrast to this, the beam quality is hardly affected by the CDR screens 2 and 3 and the off-axis screen 4. The CDR screens produce radiation up to a few THz but no visible or near-infrared light (see Part I). They are useful for beam diagnostics during FEL operation. The off-axis screen 4 is particularly valuable as it permits high-resolution diagnostics on a single bunch out of a long train without affecting the SASE efficiency of the unkicked bunches. A photo of the screen holder is shown in Fig. 14.

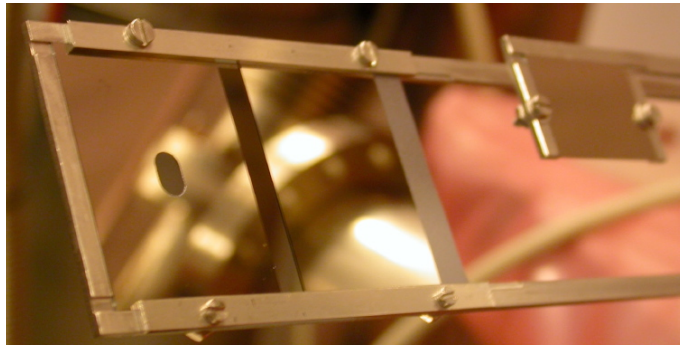


Figure 14: *Photo of the screen holder with the CDR screen 2 at the left side, the CTR screen 1 in the center and the off-axis screen 4 at the right side.*

### 4.3 Suppression of waveguide effects in the beam pipe

The THz beam pipe is made from stainless steel. The diameter has been chosen as large as possible taking into account the constraints given by the tube traversing the shielding wall of the accelerator. The diameter of the THz pipe is about 200 mm except at the beginning and the end of the beamline where the THz beam has a smaller cross section due to focusing and fits well into a 100 mm tube. The most critical part is the 9 m long section inside the shielding wall. At the end of this section the outer rim of a low-frequency THz beam ( $f \leq 300 \text{ GHz}$ ) hits the beam pipe. An important design goal was to prevent reflections at the metallic wall because these could easily destroy the narrow time profile of the THz pulse. The first idea was to cover the pipe wall with a microwave

absorbing material, however it turned out to be impossible to find a material with a high absorption at glancing incidence angles and in a broad frequency band from 200 GHz to 50 THz, which moreover was suitable for vacuum.

A very elegant alternative solution was found: using stainless steel bellows instead of tubes with a smooth wall, all electromagnetic waves with a significantly shorter wavelength than the corrugation length should undergo chaotic scattering at the wall of the bellows and should thereby be prohibited from propagating in a waveguide mode. This idea was experimentally checked with infrared light from a laser diode and with thermal radiation from a soldering iron. The radiation source was placed at a distance of 4 m from a pyroelectric detector. A chopped beam was used to remove environmental background. With free-space propagation the signal was barely visible above the noise level. Inserting a stainless steel pipe of 200 mm inner diameter between source and detector yielded a strong enhancement of the signal, implying that the smooth pipe acted as a wave guide for the infrared radiation. In the next step the smooth pipe was replaced by a bellows of 192 mm inner diameter. In this case, the observed signal was not enhanced but remained as small as in the free-space propagation case. This demonstrates that bellows have basically no wave guide effect for wavelengths that are much shorter than its corrugation length. In a final experiment a 10 GHz microwave transmitter ( $\lambda = 30 \text{ mm} > \ell_{corr} = 16 \text{ mm}$ ) was used as a source. Here the bellows showed the same wave-guide enhancement of the detector signal as the smooth pipe. This is intuitively clear because the long-wavelength radiation averages over the corrugations.

## 4.4 Mirrors

All mirrors deflect the beam by  $90^\circ$ . They have an elliptical contour to appear as circular mirrors when viewed along the beam direction. The focusing mirrors F1 to F4 are toroids with a ratio of 1:2 of the radii (see Part I). The focal lengths and the dimensions are listed in Table 1. These mirrors were manufactured by the company LT Ultra-Precision Technology from massive steel resp. aluminum-alloy plates with precision diamond tooling. The specified surface roughness is  $R_a \leq 10 \text{ nm}$ , the average deviation from the ideal surface contour is  $\leq 0.5 \mu\text{m}$  in the center region of the mirrors and  $\leq 5 \mu\text{m}$  near the rim. Mirror F5 is an off-axis paraboloid and was manufactured by Kugler Precision. All mirrors are hard-plated with gold and feature a very high reflectivity in the THz regime (the specified values at  $10.6 \mu\text{m}$  and  $45^\circ$  incidence angle are 99.4% for S polarization and 98.5% for P polarization). The micromovers of the mirrors F1, F2, F3, F4 and P3 are

mirror	F1	F2	F3	F4	F5
focal length [mm]	620	4500	3500	3000	200
diameter [mm]	140	190	190	140	94

Table 1: *Focal lengths and diameters (as seen by the incident beam) of the toroidal mirrors in the THz beamline.*

equipped with stepping motors to facilitate remotely controlled optical alignment of the beamline in the evacuated state.

## 4.5 Optical imaging and diffraction along the beamline

In Sect. 2 we have presented the computed diffraction patterns of transition radiation in a simplified beamline, equipped with ideal lenses. The program *THzTransport* has been used to compute the propagation of transition radiation through the real beamline, containing the wedge-shaped diamond window, five toroidal and four plane mirrors. Also the  $45^\circ$  inclination angle of the radiation screen and its rectangular shape are taken into account. The computed intensity patterns at selected positions are shown in Fig. 15 for a frequency of 200 GHz. Although the overall appearance is similar to the idealized case of Fig. 5, one can observe distinct deviations from the cylindrical symmetry seen in that figure. Most of the asymmetries are due to the prism effect of the wedge-shaped diamond window. The acceptance limitation at 200 GHz is again given by the focusing mirror F3 at the end of the 9 m long beam pipe traversing the shielding wall. Already at 300 GHz

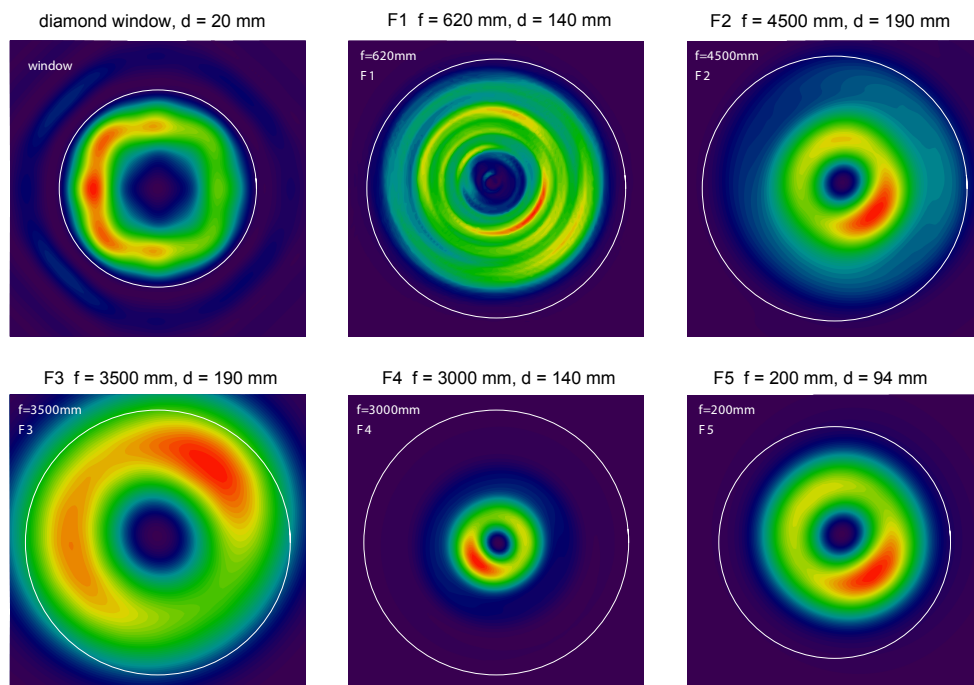


Figure 15: *The two-dimensional intensity distributions of transition radiation at the diamond window and the five focusing mirrors. The circles represent the apertures of the mirrors as seen by the incident beam, their focal lengths  $f$  and diameters  $d$  are listed above the pictures. The generation and propagation of transition radiation has been modeled using the program *THzTransport*. The Lorentz factor of the electrons is  $\gamma = 1000$ . The frequency is 200 GHz.*

the beam width is considerably reduced, see Fig. 16.

## 4.6 Energy transmission of the THz beamline

An important aim in designing the THz beamline was to obtain a large transmission efficiency for electromagnetic radiation over a wide wavelength range. We have already

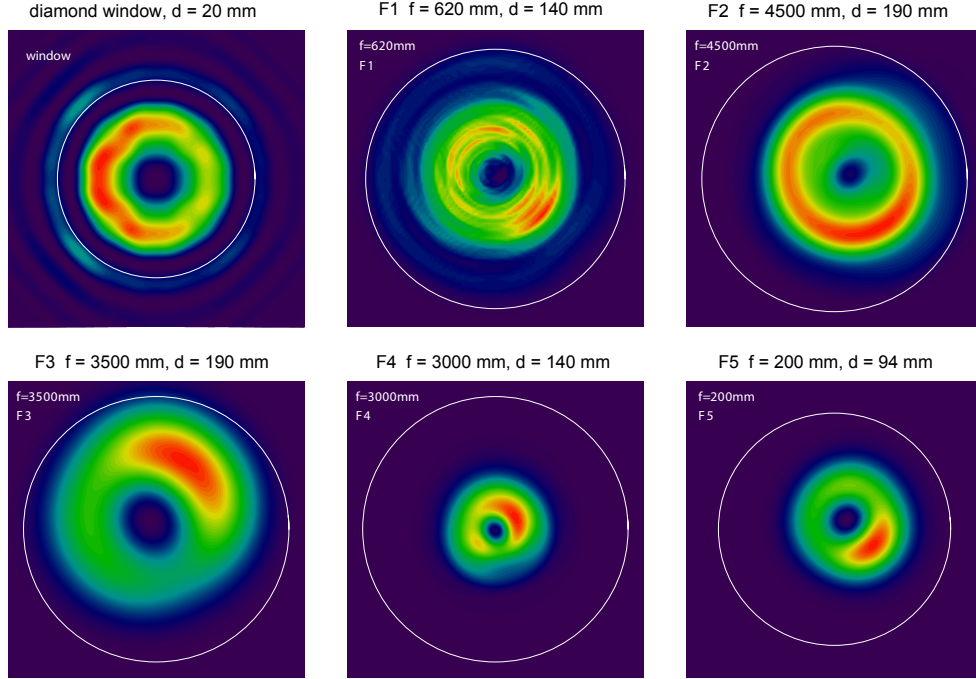


Figure 16: *The two-dimensional intensity distributions of transition radiation at the window and the five focusing mirrors for a frequency of 300 GHz.*

shown in Sect. 2 that the beam pipe diameter of 192 mm sets a lower frequency limit of about 200 GHz. We consider first the aperture limitation given by the diamond window and the first focusing mirror F1, and compute then the absolute spectral energy which is expected at the end of the THz beamline.

#### 4.6.1 Geometric acceptance of diamond window and mirror F1

The diamond window constitutes the first aperture of the THz beamline. The question is whether the small size of this window determines the angular acceptance of the beamline. In order to investigate this question in a semi-analytic way we consider first the simplified case of backward transition radiation from a circular CTR screen of 12.5 mm radius. The influence of the 45° inclination angle of the CTR screen and its rectangular shape are studied in the next section. The acceptance angle of the window is  $\theta_w = \arctan(r_w/D_w) = 14^\circ$  where  $r_w = 10$  mm is the radius of the window and  $D_w = 40$  mm its distance from the radiation screen. If we consider an aperture subtending the solid angle of the window at a large distance from the TR source (in the far-field of diffraction), then the fraction of CTR energy within this solid angle would be

$$\eta_w = \frac{\int_0^{\theta_w} U_{GF}(\theta) 2\pi \sin \theta d\theta}{\int_0^{\pi/2} U_{GF}(\theta) 2\pi \sin \theta d\theta} \quad (8)$$

where  $U_{GF}(\theta) \equiv \frac{d^2U_{GF}}{d\omega d\Omega}$  stands for the Ginzburg-Frank distribution. For a Lorentz factor  $\gamma = 1000$  one obtains  $\eta_w = 0.71$ . The first focusing mirror F1 has a radius of 70 mm and is placed at a distance of 600 mm from the TR screen. The fraction of CTR energy inside the mirror aperture is  $\eta_{F1} = 0.60$  in the far-field approximation.

Two modifications are needed:

(1) The CTR screen is not an infinite plane but has a finite size, in the present simplified treatment it is assumed to be a circular disk of radius  $a = 12.5$  mm.

(2) The window is at a very close distance to the source.

In Part I we have derived the modifications caused by the finite screen size and the near-field diffraction effects. We consider here a point-like electron bunch with a charge of 0.1 nC (number of electrons  $N_e = 6.2 \cdot 10^8$ ). This is typically the charge contained in the sharp front peak of the electron bunches in the linac of the VUV-FEL. Coherent transition radiation on a circular screen of radius  $a$  is described by the generalized Ginzburg-Frank formula (see Eq. (20) in Part I):

$$\begin{aligned} \frac{d^2U}{d\omega d\Omega} &= \frac{(N_e e)^2}{4\pi^3 \epsilon_0 c} \cdot \frac{\beta^2 \sin^2 \theta}{(1 - \beta^2 \cos^2 \theta)^2} [1 - T(\theta, \omega)]^2 \\ T(\theta, \omega) &= \frac{\omega a}{c\beta\gamma} J_0\left(\frac{\omega a \sin \theta}{c}\right) K_1\left(\frac{\omega a}{c\beta\gamma}\right) + \frac{\omega a}{c\beta^2\gamma^2 \sin \theta} J_1\left(\frac{\omega a \sin \theta}{c}\right) K_0\left(\frac{\omega a}{c\beta\gamma}\right) \end{aligned}$$

By numerical integration of this formula over the backward hemisphere we obtain the total spectral energy radiated by the bunch:

$$U_{tot}(\omega) = 2\pi \int_0^{\pi/2} \frac{d^2U}{d\omega d\Omega} \sin \theta d\theta$$

This spectral energy density is plotted in Fig. 17 as a function of frequency for a CTR screen radius  $a = 12.5$  mm and a Lorentz factor  $\gamma = 1000$ . The frequency interval is chosen as  $\Delta f = 100$  GHz. The spectral energy amounts to about  $U_{tot} = 0.45 \mu\text{J}/(100 \text{ GHz})$  at 100 GHz and rises with increasing frequency until it approaches above 5 THz the value of  $U_{GF} = 0.85 \mu\text{J}/(100 \text{ GHz})$  which is computed from the angle-integrated Ginzburg-Frank formula (see Eq. (30) in Part I):

$$U_{GF}(\omega) \equiv \left(\frac{dU}{d\omega}\right)_{GF} = \frac{(N_e e)^2}{2\pi^2 \epsilon_0 c} \ln \gamma$$

In the next step we compute the energy flow through the window in the near-field regime. The radial distribution of the transition radiation intensity at the window aperture can be calculated by numerical integration of formula (25) in Part I:

$$\frac{d^2U}{d\omega d\Omega} \propto \left| \int_0^a J_1(k\rho \sin \theta) K_1\left(\frac{k\rho}{\beta\gamma}\right) \exp\left(ik\frac{\rho^2}{2R}\right) \rho d\rho \right|^2$$

The results are shown in Fig. 18 for 500 GHz and 1 THz. A second numerical integration is used to compute the energy  $U_{win}(\omega)$  passing through the window aperture. Normalizing to the total radiated energy  $U_{tot}(\omega)$  we obtain the acceptance of the window

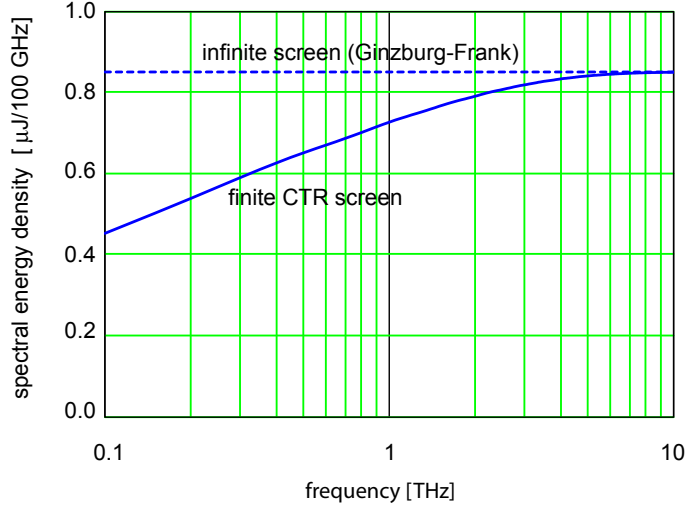


Figure 17: Total spectral energy density  $U_{tot}$  of coherent transition radiation which is emitted by a point-like electron bunch (charge 0.1 nC) upon crossing a circular CTR screen of 12.5 mm radius. The dashed line shows the spectral energy density  $U_{GF}$  obtained from an infinite CTR screen.

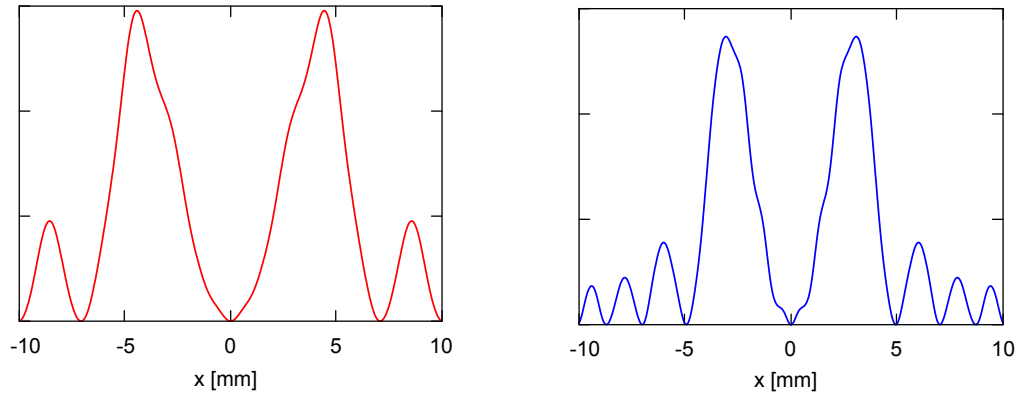


Figure 18: Horizontal cut through the CTR intensity pattern on the diamond window for  $f = 500$  GHz (left plot) resp. 1 THz (right plot). The interference rings are caused by the finite size of the CTR screen (radius  $a = 12.5$  mm). A similar picture for  $f = 200$  GHz has already been shown in Fig. 13.

$\eta_{win}(\omega) = U_{win}(\omega)/U_{tot}(\omega)$  which is plotted in Fig. 19 as a function of the normal frequency  $f = \omega/(2\pi)$ . This acceptance rises from about 0.35 at 100 GHz to the asymptotic value of 0.71 above 5 THz, given by Eq. (8). Note that the window material itself is neglected here, so there are no reflection losses.

Next we study the limitation given by the focusing mirror F1 with a radius of  $r_{F1} = 70$  mm and at a distance  $D_{F1} = 600$  mm from the TR screen. In this simulation the aperture limitation by the diamond window is disregarded. The computed energy transmission

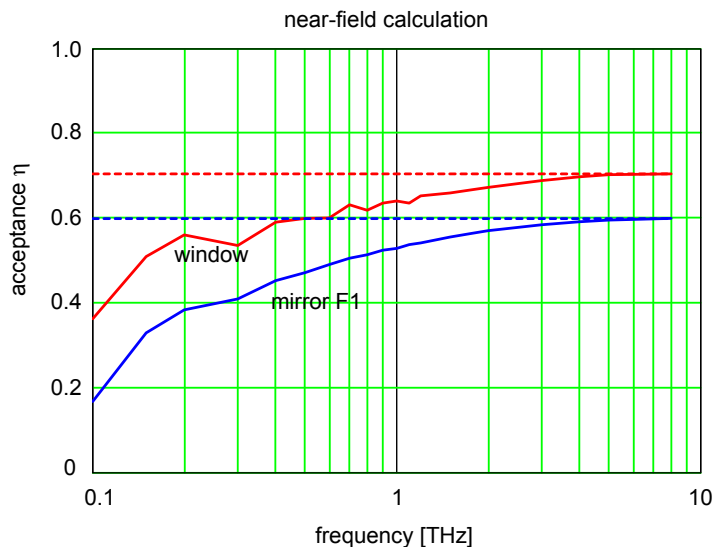


Figure 19: *Frequency-dependent acceptance of the diamond window (red curve) resp. the mirror F1 (blue curve) for coherent transition radiation from a circular screen of 12.5 mm radius. The plateau values of 71% for the window and 60% for the mirror F1 are reached at frequencies above 5 THz. It is obvious that the mirror constitutes the tighter acceptance limitation.*

through the aperture of the mirror is also shown in Fig. 19. From this figure it is obvious that the mirror F1 has a smaller angular acceptance than the diamond window. Hence an enlargement of the window would not improve the acceptance of the THz beamline.

It is interesting to note that the aperture limitation caused by the mirror F1 is even effective at optical frequencies where the wavelengths are many orders of magnitude smaller than the mirror dimensions. Only for frequencies below 1 THz the mirror F3 (located behind the 9 m long beamline section crossing the shielding wall of the accelerator) constitutes a tighter acceptance limitation, see also Fig. 15. Another remarkable observation is that the far-field and the near-field calculations lead to rather similar results for the energy flow through the free aperture of the diamond window resp. the mirror F1.

#### 4.6.2 Energy transfer through the optical system

The transmission of the CTR pulse energy through the entire THz beamline has been computed with the code *THzTransport* for a point-like electron bunch with a charge of 0.1 nC. In this realistic computation all elements of the beamline have been taken into account:

- the rectangular shape of the CTR screen and its  $45^\circ$  inclination angle with respect to the incident electron beam
- the reflection losses of about 29% in the diamond window as well as the multiple reflections and the prism effect in the wedge-shaped window
- the aperture limitations given by all plane and focusing mirrors

- the optical aberrations of the toroidal mirrors F1 to F4 and the parabolic mirror F5

The spectral CTR pulse energy density behind the diamond window and at the focal plane of the last mirror (F5) is plotted in Fig. 20 as a function of frequency resp. wavelength.

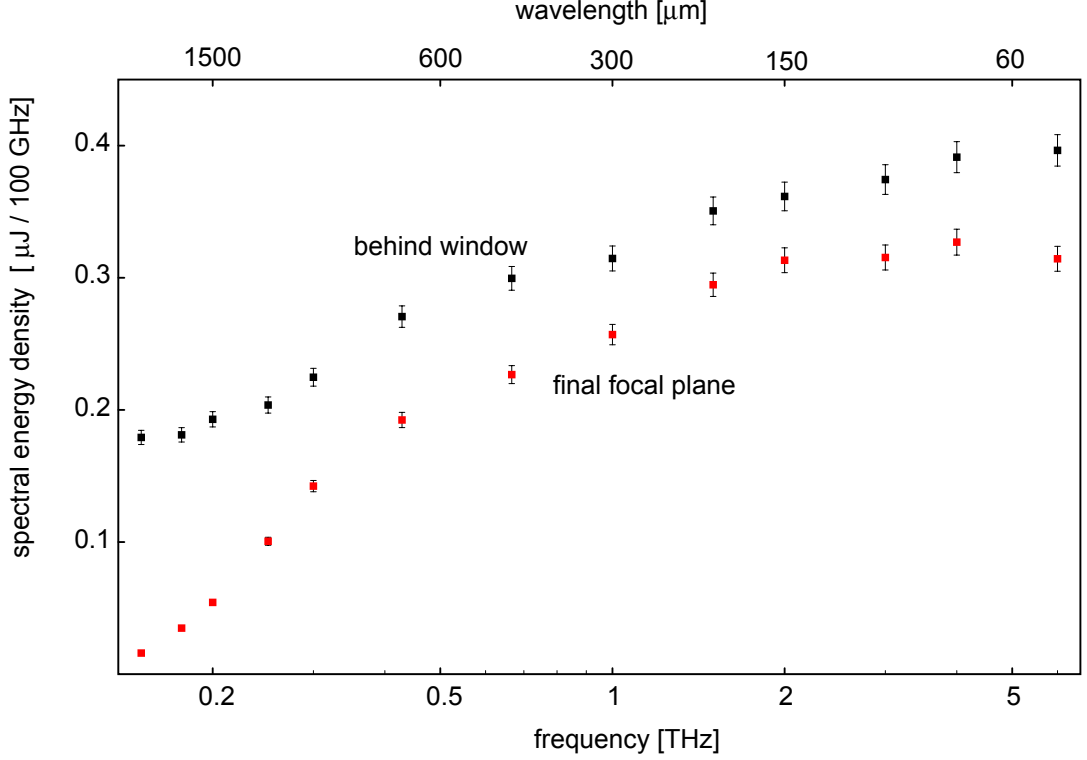


Figure 20: The spectral CTR pulse energy density in  $\mu\text{J}/(100 \text{ GHz})$  from a  $0.1 \text{ nC}$  bunch as a function of frequency. Black points: pulse energy behind the diamond window; red points: pulse energy at the final focal plane of the THz beamline. The Lorentz factor is  $\gamma = 1000$ .

The transmitted spectral energy density rises from a value of  $0.05 \mu\text{J}/(100 \text{ GHz})$  at 200 GHz to a plateau of  $\approx 0.3 \mu\text{J}/(100 \text{ GHz})$  at frequencies above 5 THz. The plateau corresponds to about 36% of the total emitted pulse energy density as computed by the Ginzburg-Frank formula. The loss at high frequencies is due to the reflection losses at the diamond window ( $\approx 29\%$ ) and the limited solid angle of the THz beamline.

Even in the visible range the limited solid angle of the THz beamline causes a significant loss although the mirrors are quite large. The reason is that the angular distribution of transition radiation is described by the Ginzburg-Frank (GF) formula for sufficiently small wavelengths ( $\gamma\lambda < a$  where  $a$  is the CTR screen radius) and becomes then independent of wavelength. The GF distribution has a wide tail. In that respect optical transition radiation is rather different from laser light.

## 5 First experimental results

The mirrors of the THz beamline were carefully aligned with laser radiation which was coupled into the optical channel through a window at the UHV chamber. Up to date a number of exploratory measurements with transition and diffraction radiation have been made, more systematic studies are underway and will be reported elsewhere.

The first and very encouraging observation is that the coherent transition radiation intensity as measured with a pyro-electric detector in the focal plane of the last mirror F5 exceeds the intensity measured with the same detector placed directly at the output window of another CTR screen in the linac, but without using a focusing mirror. Hence the transmission of the THz beamline appears to be very satisfactory. However, a quantitative evaluation of the transfer function is presently not at all straightforward because of the rather poorly known spectral response of commercially available pyro-electric detectors. An R&D project is underway together with an industrial company to produce dedicated pyro-electric sensors with a flat spectral response in the THz regime. There is a strong incentive to reduce the strong etalon-type resonances of existing detectors which are caused by reflections of the THz wave at the front and back surface of the crystal.

Two-dimensional scans have been made in the focal plane of the last mirror F5 to investigate the radiation intensity distribution. Preliminary data are shown in Fig. 21. The agreement between measurement and theory is quite satisfactory.

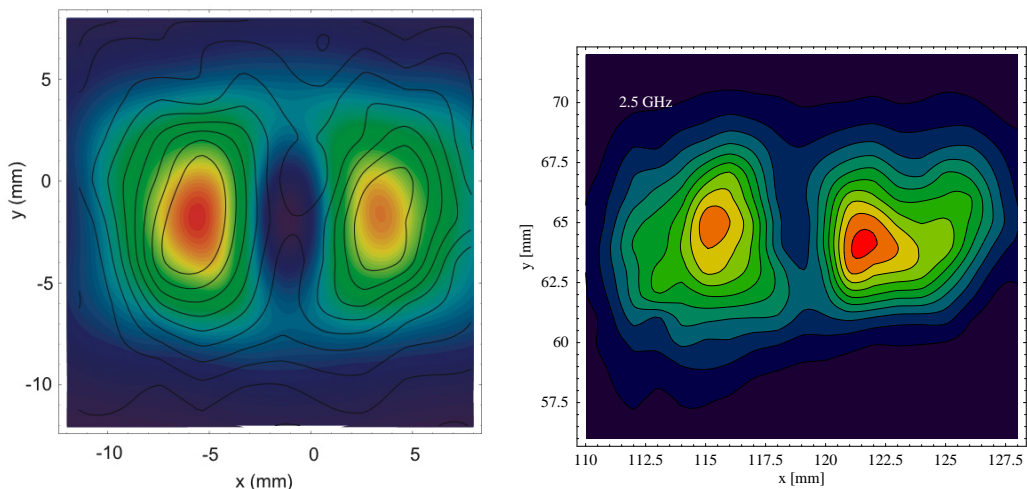


Figure 21: *Left: Intensity distribution of 800 GHz diffraction radiation in the focal plane of mirror F5. The slit-type diffraction radiator was used and a band pass filter with a spectral transmission of  $800 \pm 50$  GHz was placed in front of the pyro-electric detector. The measured intensity is indicated by the curves, the theoretical intensity distribution according to the code *THzTransport* is represented by the colour code. Right: Picture of 2.5 THz diffraction radiation in the focal plane of mirror F5.*

Experiments aimed at directly observing the temporal profile of the CTR pulse, using single-shot electro-optic detection, were undertaken by a collaboration between FELIX

FEL facility, University of Dundee, CCLRC Daresbury laboratory and DESY [11]. Preliminary measurements at the focal point of mirror F5 are shown in Fig. 22. The narrow temporal width of the observed THz pulse is evidence for the isochronous character of the THz beamline.

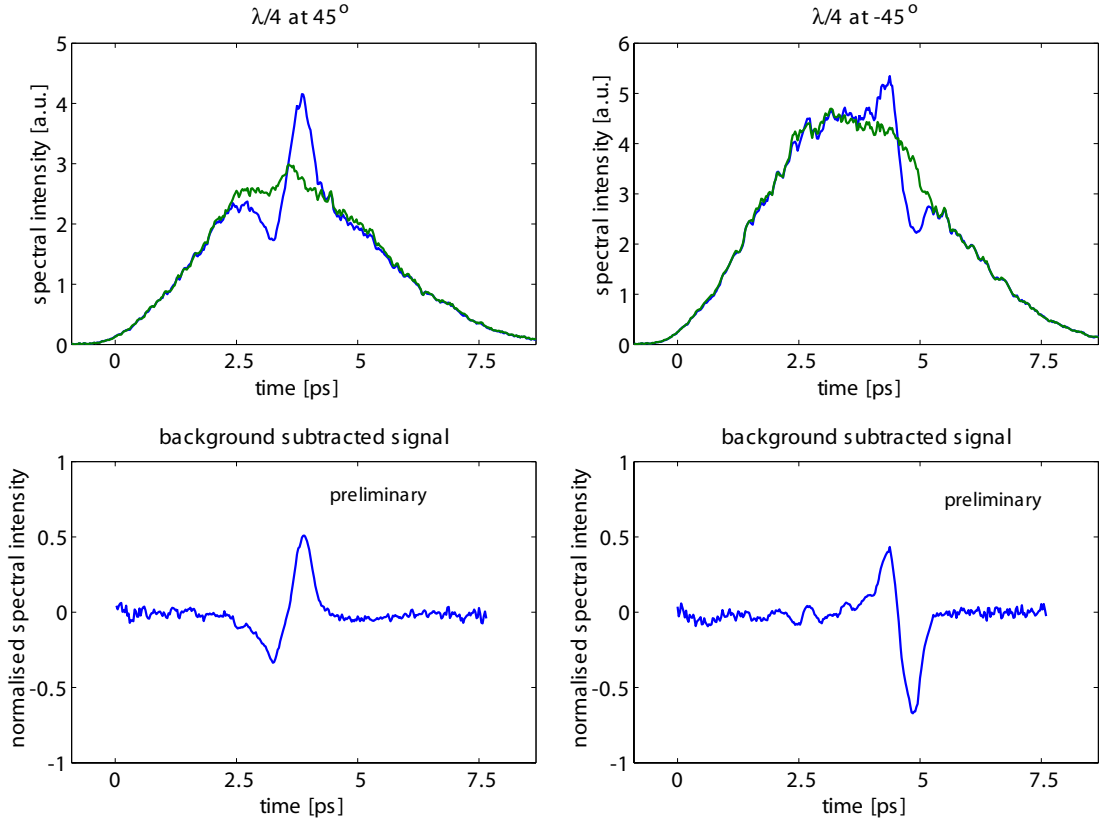


Figure 22: *Single-shot electro-optic signals obtained at the THz beamline with two different orientation angles of the quarter wave plate behind the ZnTe crystal. Top row: raw data with THz pulse (blue) and without THz pulse (green). Bottom row: EO signals after background subtraction and normalization. These preliminary experimental results were obtained as part of the FD3 collaboration [11].*

We thank our engineers O. Peters, J. Hauschildt and K. Ludwig for their help in designing the mechanical parts and the vacuum system of the THz beamline.

## References

- [1] F. Stulle, *A Bunch Compressor for Small Emittances and High Peak Currents at the VUV Free-Electron Laser*, DESY-THESIS-2004-041 (2004).
- [2] S. Casalbuoni, B. Schmidt and P. Schmüser, *Far-Infrared Transition and Diffraction Radiation Part I: Production, Diffraction Effects and Optical Propagation*, TESLA Report 2005-15 (2005).
- [3] P. Dore et al., *Infrared properties of chemical-vapor deposition polycrystalline diamond windows*, *Appl. Opt.*, **37**, 5731 (1998).
- [4] E. Palik, *Handbook of Optical Constants of Solids*, Academic Press, Inc., [http://csic.sw.edu.es/jga/tmp/OptConst\\_Palik.dat](http://csic.sw.edu.es/jga/tmp/OptConst_Palik.dat) .
- [5] P. U. Jepsen, Private communication, Departement of Molecular and Optical Physics, University of Freiburg, 2003.
- [6] Bernhard Schmidt, *THzTransport*, [www.desy.de/~schmidt/THzTransport/THzTransport.m](http://www.desy.de/~schmidt/THzTransport/THzTransport.m) .
- [7] ZEMAX, Optima Research Ltd, [www.zemax.com](http://www.zemax.com) .
- [8] J. W. Goodman, *Introduction to Fourier Optics*, McGraw-Hill, New York, 1968.
- [9] G. N. Lawrence, *Optical modeling*, vol. 11 of *Applied Optics and Optical Engineering*, Academic, San Diego, Calif., 1992.
- [10] *ZEMAX Users Manual*, ZEMAX Development Corporation, March 2004.
- [11] FELIX/Dundee/Daresbury/DESY (FD3) collaboration on Electro-Optic Techniques, G. Berden, A.F.G. van der Meer, S.P. Jamison, A.M. Gillespie, W.A.G. Macleod, B. Steffen, E.-A. Knabbe, B. Schmidt, P. Schmüser, H. Schlarb